

# A Nonconservative Flow Field for Robust Variational Image Segmentation

Pratim Ghosh, *Student Member, IEEE*, Luca Bertelli, *Student Member, IEEE*, Baris Sumengen, and B. S. Manjunath, *Fellow, IEEE*

**Abstract**—We introduce a robust image segmentation method based on a variational formulation using edge flow vectors. We demonstrate the nonconservative nature of this flow field, a feature that helps in a better segmentation of objects with concavities. A multiscale version of this method is developed and is shown to improve the localization of the object boundaries. We compare and contrast the proposed method with well known state-of-the-art methods. Detailed experimental results are provided on both synthetic and natural images that demonstrate that the proposed approach is quite competitive.

**Index Terms**—Active contours models, edge flow fields, image segmentation, nonconservative vector fields.

## I. INTRODUCTION

IMAGE segmentation is one of the widely studied problems in image processing and has found its application directly or indirectly in tasks such as object detection [11], [18], object tracking and recognition [1], [5], content-based image retrieval, and medical image analysis [22].

The Active Contours approach is one particular image segmentation technique that was originally introduced by Kass *et al.* [9], and further developed by the work of Caselles [2] and Malladi [15]. Concurrently, Kichenassamy *et al.* [10] proposed an Active Contours model based on the geometry of the image. The basic idea in this Active Contours method lies in deforming a contour according to some cost function, which upon minimization guides it towards the boundary of the object of interest. The cost function usually consists of two terms: one that maintains the smoothness of the curve, commonly known as the internal force; and another that pushes the curve towards the boundaries, known as the external force. The goodness of the segmentation result depends on how the two forces are derived from the image data.

In recent years, much progress has been made to improve the original Active Contours framework in achieving robustness

Manuscript received December 01, 2008; revised September 14, 2009. First published October 06, 2009; current version published January 15, 2010. This work was supported by the National Science Foundation Information Technology Research Grant #ITR-0331697. The associate editor coordinating the review of this manuscript and approving it for publication was Prof. Peyman Milanfar.

P. Ghosh, L. Bertelli, and B. S. Manjunath are with the Vision and Research Laboratory, Department of Electrical and Computer Engineering, University of California Santa Barbara, Santa Barbara, CA, 93106 USA (e-mail: pratim@ece.ucsb.edu; lbertelli@ece.ucsb.edu; sumengen@ece.ucsb.edu; manj@ece.ucsb.edu).

B. Sumengen is with Like.com, San Mateo, CA 94403 USA.  
Digital Object Identifier 10.1109/TIP.2009.2033983

to contour initialization [6], [12], [27], and dealing with concavities in object boundaries [27], [30], [31]. For example, in the Gradient Vector Flow (GVF) method [31] robustness to initialization is obtained by diffusion of the edge field. However, the performance of edge field-based methods in the presence of nearby boundaries is not well understood.

In recent years, there has been considerable work on region-based segmentation [3], [4], [19]. Paragios *et al.* [19] proposed supervised texture segmentation by combining both region and edge-based terms. Zhu *et al.* [32] designed a multiband image segmentation algorithm by minimizing a generalized Bayesian criterion. Recently, other approaches [13], [26] have been developed incorporating the shape and appearance information. A comprehensive discussion of the edge-based versus region-based methods is beyond the scope of this paper. Whether region-based methods are better than edge-based ones is a debatable and often a philosophical issue. However, it is generally acknowledged that the edge-based methods often provide better boundary localization, see [19], [29] for some recent work.

In this paper we present a robust image segmentation method and demonstrate its application to both synthetic and natural images. We begin by considering an edge field that was originally developed by Ma *et al.* [14] and we refer to this as the EdgeFlow Vector (EFV) field in the following discussion. The motivation for considering the EFV comes from its nonconservative<sup>1</sup> nature derived entirely from the image data. This is in contrast with the GVF where the nonconservative property is due to the addition of a smoothing term to a purely image-based component, which may affect edge localization.

The key contributions of this paper are summarized below.

- We develop an effective segmentation technique based on an edge field computed directly from the images. The flow field can be computed from various image features including color, texture and intensity edges.
- We show analytically that this edge flow field is nonconservative in nature. This is further validated by using a numerical technique called Helmholtz-Hodge Decomposition (HHD). A new edge function, more precise than the commonly used inverse of the gradient magnitude for localizing edges, is also proposed based on the scalar potential of the edge flow field.
- We further study and compare the flow field vectors derived from EFV with those of the GVF, Generalized GVF (GGVF) [30] and Magnetostatic Active Contour (MAC) [29]. This study reveals that for the segmentation of images

<sup>1</sup>Nonconservative refers to having both non zero irrotational (curl-free) and solenoidal (divergence-free) components.

with *multicontrast* edges, the edge flow method is more effective than these state-of-the-art approaches.

The rest of the paper is organized as follows. Section II reviews the prior work on edge flow fields. In Section III, we formulate the segmentation problem using this edge flow field within a curve evolution framework. The Helmholtz Hodge decomposition is used to study the characteristics of this vector edge flow field. We also provide an extensive analysis of the nonconservative property of EFV. A detailed comparison with GVF and GGVF is presented in Section IV. Section V provides experimental results, and we conclude in Section VI.

## II. REVIEW OF PRIOR WORK ON EDGE FLOW FIELDS

Since the development of Active Contours for image segmentation, there has been considerable work on generating “edge flow” vectors that drive the detected edges towards the true object boundaries in the image. Cohen and Cohen [6] proposed a flow field, the Distance Vector Flow, based on the Chamfer distance transform of binary edge images. Caselles *et al.* [2] derived a flow field by taking the gradient of a scalar function ( $h = 1/(1 + |\nabla I_\sigma|)$ , where  $I_\sigma$  is a Gaussian convolved image) which is small on the edges and large away from the edges. In [8], Gil and Radeva designed a new distance transform based on the curvature information of the curve to be modeled. The gradient map of this distance transform, known as CVF (Curvature Vector Flow), is then used as the flow field for segmentation. Xie *et al.* [29] developed a flow field based on magnetostatic interactions between the Active Contours and the object boundaries. The algorithm was shown to be robust in terms of initialization on a variety of images having complex structures. Xu and Prince proposed GVF [31], one of the more widely used edge flow fields. Further variants of the basic GVF framework can be found in [20], [30]. The basic GVF field  $\mathbf{G}(x, y) = [g_1(x, y), g_2(x, y)]$  is obtained by minimizing the following functional:

$$\int \int \mu (g_{1x}^2 + g_{1y}^2 + g_{2x}^2 + g_{2y}^2) + |\nabla f|^2 |\nabla f - \mathbf{G}(x, y)|^2 dx dy \quad (1)$$

where  $g_{px} = (\partial g_p / \partial x)|_{p=1,2}$  and  $g_{py} = (\partial g_p / \partial y)|_{p=1,2}$ . Also, note that  $|\nabla f|$  is high near the edges and nearly zero in homogeneous regions and  $\mu$  is the regularization parameter. In [31],  $f(x, y)$  is chosen to be  $I(x, y)$ , i.e., the image itself. Using calculus of variation, the minimization of (1) reduces to solving the following system of Euler equations:

$$\begin{aligned} \mu \nabla^2 g_1 - (g_1 - f_x)(f_x^2 + f_y^2) &= 0 \\ \mu \nabla^2 g_2 - (g_2 - f_y)(f_x^2 + f_y^2) &= 0 \end{aligned} \quad (2)$$

where  $f_x = (\partial f / \partial x)$  and  $f_y = (\partial f / \partial y)$ . This  $\mathbf{G}(x, y)$  field is controlled by  $|\nabla I|$  near the edges. In the homogenous regions of the images,  $\mathbf{G}(x, y)$  is slowly varying and points towards the edges due to the smoothing term [the first term in (1)]. The combination of the smoothing and gradient terms makes this GVF field nonconservative (see Section IV). GGVF [30] extends the basic GVF by introducing two spatially varying terms instead of  $\mu$  and  $|\nabla f|^2$  in (1). The introduction of such terms reduces

undesired smoothing effect near strong edges. The Euler equation corresponding to GGVF is

$$\eta_1 \nabla^2 \tilde{\mathbf{G}} - \eta_2 (\tilde{\mathbf{G}} - \nabla f) = 0 \quad (3)$$

where  $\tilde{\mathbf{G}}(x, y) = [\tilde{g}_1(x, y), \tilde{g}_2(x, y)]$  is the GGVF field, and  $\eta_1$  and  $\eta_2$  are the two spatially varying terms that replace  $\mu$  and  $|\nabla f|^2$  respectively in (1). In [30], the authors used

$$\eta_1 = e^{-(|\nabla f|/K)} \quad \text{and} \quad \eta_2 = 1 - \eta_1$$

where  $K$  controls the smoothing effect in the extracted field.

### A. EdgeFlow Vector Field (EFV)

In a similar spirit, Ma and Manjunath [14] introduced the EFV vectors. The magnitude and direction of the EFV vectors are estimated using the intensity gradient magnitude ( $\mathbf{E}_{\text{grad}}$ ) and the prediction errors ( $\mathbf{E}_{\text{pred}}$ ). For an image  $I(x, y)$ , the  $\mathbf{E}_{\text{grad}}$  and  $\mathbf{E}_{\text{pred}}$  at a particular location  $\mathbf{r} = (x, y)$  along the orientation  $\theta$  are computed as

$$\begin{aligned} \mathbf{E}_{\text{grad}}(\mathbf{r}, \sigma, \theta) &= |\nabla_\theta I_\sigma(x, y)| \\ \mathbf{E}_{\text{pred}}(\mathbf{r}, \sigma, \theta) &= |I_\sigma(x + d \cos \theta, y + d \sin \theta) - I_\sigma(x, y)| \end{aligned} \quad (4)$$

where  $I_\sigma$  is the Gaussian smoothed image;  $d$  (offset parameter) is the distance of the prediction<sup>2</sup> and is usually set to  $4\sigma$ .  $\mathbf{E}_{\text{grad}}(\mathbf{r}, \sigma, \theta)$  calculates the strength of intensity change along the orientation  $\theta$  at a location  $\mathbf{r}$ . In contrast,  $\mathbf{E}_{\text{pred}}(\mathbf{r}, \sigma, \theta)$  computes the error in predicting the neighbor along the orientation  $\theta$  using the image information at  $\mathbf{r}$ . Thus,  $\mathbf{E}_{\text{pred}}$  is small if the neighbor belongs to the same object. Note that finding the gradient magnitude and the prediction error is equivalent to convolving the image with the first derivative of Gaussian (DG) and the difference of offset Gaussian (DOOG) filters. Examples of the DG and the DOOG kernels are presented in the Fig. 1. The difference between DOOG and DG is that the former is asymmetric whereas the latter one is a symmetric operator. This property of DOOG, unlike DG, makes it sensitive to the directions  $\theta$  and  $\theta + \pi$ , as shown in the contour plots in Fig. 1(c) and (d).

Now we define the edge likelihood function  $P$  at a particular direction  $\theta$  using the relative prediction errors  $\mathbf{E}_{\text{pred}}(\mathbf{r}, \sigma, \theta)$  and  $\mathbf{E}_{\text{pred}}(\mathbf{r}, \sigma, \theta + \pi)$  as follows:

$$P(\mathbf{r}, \sigma, \theta) = \frac{\mathbf{E}_{\text{pred}}(\mathbf{r}, \sigma, \theta)}{\mathbf{E}_{\text{pred}}(\mathbf{r}, \sigma, \theta) + \mathbf{E}_{\text{pred}}(\mathbf{r}, \sigma, \theta + \pi)}. \quad (6)$$

The above  $P(\mathbf{r}, \sigma, \theta)$  needs to be smoothed before searching for the most probable orientation  $\hat{\theta}$  for the flow direction. We do this by integrating  $P$  over the interval  $(\theta - (\pi/2), \theta + (\pi/2))$ . Define  $\hat{P}(\mathbf{r}, \sigma, \theta)$  as

$$\hat{P}(\mathbf{r}, \sigma, \theta) = \int_{\theta - \pi/2}^{\theta + \pi/2} P(\mathbf{r}, \sigma, \theta') d\theta'. \quad (7)$$

Then the probable flow direction  $\hat{\theta}$  at  $\mathbf{r}$  is estimated as

$$\hat{\theta}(\mathbf{r}, \sigma) = \underset{\theta}{\operatorname{argmax}} \hat{P}(\mathbf{r}, \sigma, \theta). \quad (8)$$

<sup>2</sup>A comprehensive overview of its effect on image segmentation is presented in Fig. 10(b).

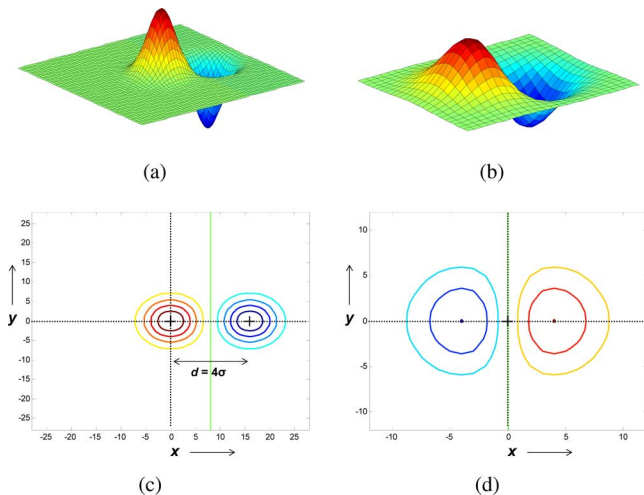


Fig. 1. This figure demonstrates the difference between the Difference of offset Gaussian (DOOG) and the first derivative of Gaussian (DG). The surface plots of (a) DOOG, (b) DG. The corresponding contour plots are shown in (c) and (d), respectively. The offset ( $d = 4\sigma$ ) of DOOG is shown by a black arrow in the contour plot (bottom left). It is to be noted that DOOG is an asymmetric operator unlike DG which is symmetric.

Finally, the EFV field is calculated as the vector sum

$$\mathbf{E}(\mathbf{r}, \sigma) = \int_{\hat{\theta} - \pi/2}^{\hat{\theta} + \pi/2} \mathbf{E}_{\text{grad}}(\mathbf{r}, \sigma, \theta) e^{i\theta} d\theta \quad (9)$$

where  $i = \sqrt{-1}$ . The  $\mathbf{E}$  obtained (for a given scale  $\sigma$ ) in (9) is a complex number whose magnitude and angle represent the resulting edge energy and the flow direction at a particular location  $\mathbf{r}$ . The EFV can be extended to multiscale analysis as well as shown in Appendix A. EFV at multiple scales helps in preserving edge localization, while extending the field to larger homogeneous regions as shown in Fig. 2. The main properties of the EFV field can be summarized as follows:

- 1) the vectors point normally towards the nearest edge;
- 2) the magnitude of the vectors is small away from the edges and increases near the edges;
- 3) the flow vectors from opposite directions cancel each other on the edges.

### III. EDGE FLOW DRIVEN CURVE EVOLUTION FRAMEWORK

A general curve evolution framework [25] is governed by the following equation:

$$\frac{\partial C}{\partial t} = \alpha F_1 + \beta F_2 + F_3 \quad (10)$$

where  $C(q) : [0, 1] \rightarrow \mathbb{R}^2$  is a parameterized planar curve;  $F_1 = a(x, y)\mathcal{N}$  ( $\mathcal{N}$  is the unit normal to the curve  $C(q)$ ) is an expansion/shrinking force;  $F_2 = a(x, y)\kappa\mathcal{N}$  is a curvature based force and  $F_3 = (\mathbf{S} \cdot \mathcal{N})\mathcal{N}$  is a force based on an underlying edge flow vector field  $\mathbf{S}$ , whose direction and strength are usually independent of the evolving curve. The function  $a(x, y)$  is expected to be small on the edges and large away from the edges. The curve is evolved in the normal direction  $\mathcal{N}$  by a combination of these forces. We would like to note that  $F_2$  is

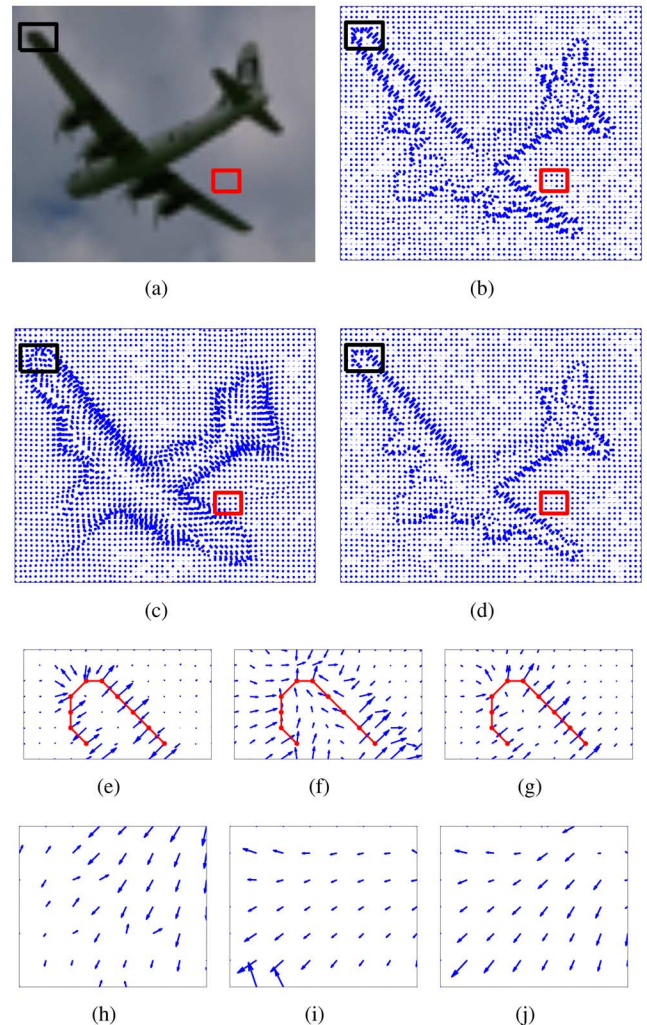


Fig. 2. This result demonstrate the effectiveness of the multiscale technique over the single scale one. (a) Image of an aeroplane. Plots of the EFV field  $\mathbf{E}$  for (b)  $\sigma = 0.5$ , (c)  $\sigma = 2$ , and (d) multiscale (from  $\sigma = 0.5$  to  $\sigma = 2$  in steps of 0.5). Two different areas corresponding to an edge region (in black rectangle) and a smooth region (in red rectangle) of each of the flow fields are enlarged for the sake of clarity; (e), (f), (g) magnify the black rectangles and (h), (i), (j) magnify the red rectangles for  $\sigma = 0.5, \sigma = 2$ , and multiscale, respectively. Note that the proposed multiscale framework is able to extract meaningful [see, e.g., similarity between (e) and (i) with (g) and (j), respectively] information from each of them.

the only term which provides stability to the level-set-based solution and thus is necessary for this formulation. However,  $F_2$  may have adverse effect in some cases, e.g., expansion of the curve near concavity, which can be tackled by proper design of other terms.

In the literature [7], a common choice for  $a(x, y)$  (known as the edge stopping function) is the inverse of the gradient magnitude function, which is small on the edges and large away from the edges. For example,  $a(x, y) = (1/1 + |\nabla I_\sigma|)$  has been used in [21], where the choice for  $\mathbf{S}$  was the GVF field  $\mathbf{G}$ . In contrast, in Geodesic Active Contour (GAC) the corresponding edge flow field was derived as the gradient of the edge stopping function  $a(x, y)$ , i.e.,  $\mathbf{S} = -\nabla a$  [2]. Alternatively, one can compute the edge flow field from the image features (intensity edges, texture, color) and derive analytically the corresponding

edge stopping function in a principled way from the flow field. Note that any function  $\phi(x, y)$  that satisfies  $\mathbf{S} = -\nabla\phi$  meets the requirement of an edge stopping function  $a(x, y)$ . We now present an approach for computing  $\phi(x, y)$  given  $\mathbf{S}$  using the Helmholtz-Hodge Decomposition [23].

#### A. Helmholtz-Hodge Decomposition

Given a smooth ( $\in C^\infty$ ), rapidly decaying vector field (e.g., EFV, GVF, or GAC) the Helmholtz theorem states that it can be resolved into conservative (curl-free) and solenoidal (divergence-free) components. Recently, it has been shown in [23] that the Helmholtz theorem can be further generalized by the Helmholtz-Hodge decomposition as follows:

$$\begin{aligned}\mathbf{S} &= \mathbf{S}_{\text{con}} + \mathbf{S}_{\text{sol}} + \mathbf{S}_{\text{har}} \\ &= -\nabla\phi + \nabla \times \mathbf{A} + \mathbf{S}_{\text{har}}\end{aligned}\quad (11)$$

where  $\mathbf{S}_{\text{con}} = -\nabla\phi$  is the conservative (curl-free) component which satisfies  $\nabla \times \mathbf{S}_{\text{con}} = 0$ ,  $\mathbf{S}_{\text{sol}} = \nabla \times \mathbf{A}$  is solenoidal (divergence-free) component which satisfies  $\nabla \cdot \mathbf{S}_{\text{sol}} = 0$ ,  $\mathbf{S}_{\text{har}}$  is the harmonic component which satisfies both  $\nabla \times \mathbf{S}_{\text{har}} = 0$  and  $\nabla \cdot \mathbf{S}_{\text{har}} = 0$ . Note that  $\phi$  and  $\mathbf{A}$  stand for scalar and vector potential of  $\mathbf{S}$ . Next, we present the two functionals whose minimization lead to the solution of scalar and vector potential [16] of the flow field.

1) *Solution for Scalar Potential  $\phi(x, y)$* : The scalar potential  $\phi$  can be obtained by projecting  $\mathbf{S}$  onto the curl-free component and solving the following variational problem:

$$\operatorname{argmin}_{\phi} \int_{\Gamma} \|\mathbf{S} + \nabla\phi\|^2 dA, \quad \Gamma \subset \mathbb{R}^2 \quad (12)$$

where  $\Gamma$  is image domain under consideration. Using calculus of variation (Appendix B) it can be shown that  $\phi$  which minimizes the above functional can be found by solving the following Poisson problem:

$$\begin{aligned}\nabla \cdot \mathbf{S} &= -\nabla^2\phi \\ (\mathbf{S} + \nabla\phi) \cdot \hat{n} &= 0 \text{ in } \partial\Gamma\end{aligned}\quad (13)$$

where  $\hat{n}$  is the unit outward normal to the boundary  $\partial\Gamma$ .

2) *Solution for Vector Potential  $\mathbf{A}$* : Similarly the vector potential  $\mathbf{A}$  can be obtained by solving the following least squares formulation:

$$\operatorname{argmin}_{\mathbf{A}} \int_{\Omega} \|\mathbf{S} - (\nabla \times \mathbf{A})\|^2 dV, \quad \Omega \subset \mathbb{R}^3. \quad (14)$$

Again one can show that the optimum solution is obtained by solving the following PDE formulation:

$$\begin{aligned}\nabla \times \mathbf{S} &= \nabla \times \nabla \times \mathbf{A} = \nabla(\nabla \cdot \mathbf{A}) - \nabla^2\mathbf{A} \\ ((\mathbf{S} - \nabla \times \mathbf{A}) \times \hat{n}) &= 0 \text{ in } \partial\Omega\end{aligned}\quad (15)$$

where  $\hat{n}$  is the unit outward normal to the boundary  $\partial\Omega$ . In (14), note that ‘‘curl’’ ( $\nabla \times$ ) is a 3-D vector operator. Thus, for an arbitrary choice of  $\mathbf{A}$  we need to extend the 2-D field  $\mathbf{S}$  (lying in the image plane) to a 3-D form by setting its third component to zero. However, here we are solving a special case where the vector potential is  $\mathbf{A} = A(x, y)\mathbf{k}$ , where  $\mathbf{k}$  is the unit vector

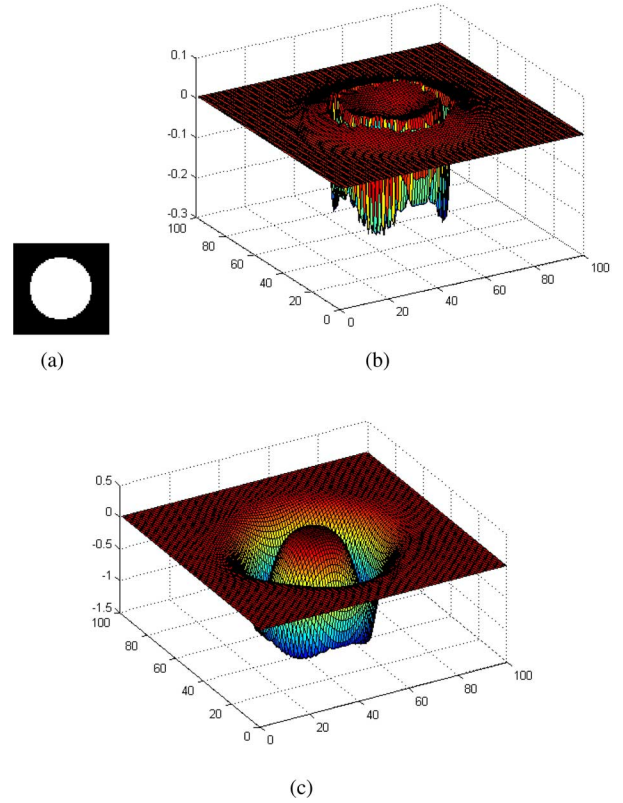


Fig. 3. (a) Example image of a circle. The plot of (b)  $\nabla \cdot \mathbf{S}$ , where  $\mathbf{S}$  is the edge flow field EFV and (c)  $\phi(x, y)$  of the example image. Note that the scalar potential function  $\phi$  is a smooth version of  $\nabla \cdot \mathbf{E}$ .

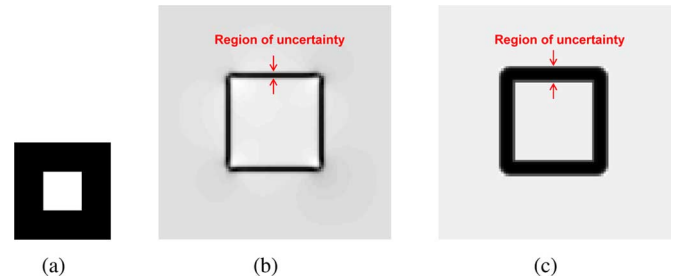


Fig. 4. (a) Example image of a square. The plot of (b)  $\phi(x, y)$  obtained from EFV and (c)  $h = (1/1 + |\nabla I_{\sigma_1}|)$  of the example image. The scale parameter  $\sigma$  is chosen to be 1 for both cases. In the plots the white region corresponds to high values ( $\approx 1$ ) whereas the black region corresponds to low values ( $\approx 0$ ).

along  $z$  direction. Thus,  $\nabla(\nabla \cdot \mathbf{A}) = 0$  and equating only the  $z$  components from the two sides, we obtain

$$(\nabla \times \mathbf{S})_z = -\nabla^2 A \quad (16)$$

where the subscript  $z$  stands for the  $z$  component of the corresponding vector. Appendix C gives the full derivation.

The PDE in the (13) gives a better insight into why  $\phi$ , derived this way, satisfies the properties of an edge stopping function. For a vector field, the divergence operator determines whether a point is a source or a sink. In the case of  $\mathbf{S}$ , the edges behave like a sink where the flow vectors meet each other. Thus, the divergence of  $\mathbf{S}$  is negative at the edges. To be specific, the profile of  $\nabla \cdot \mathbf{S}$  [Fig. 3(b)] is generally rough with distinct local minima at the edges. Using this PDE to solve for  $\phi$ ,

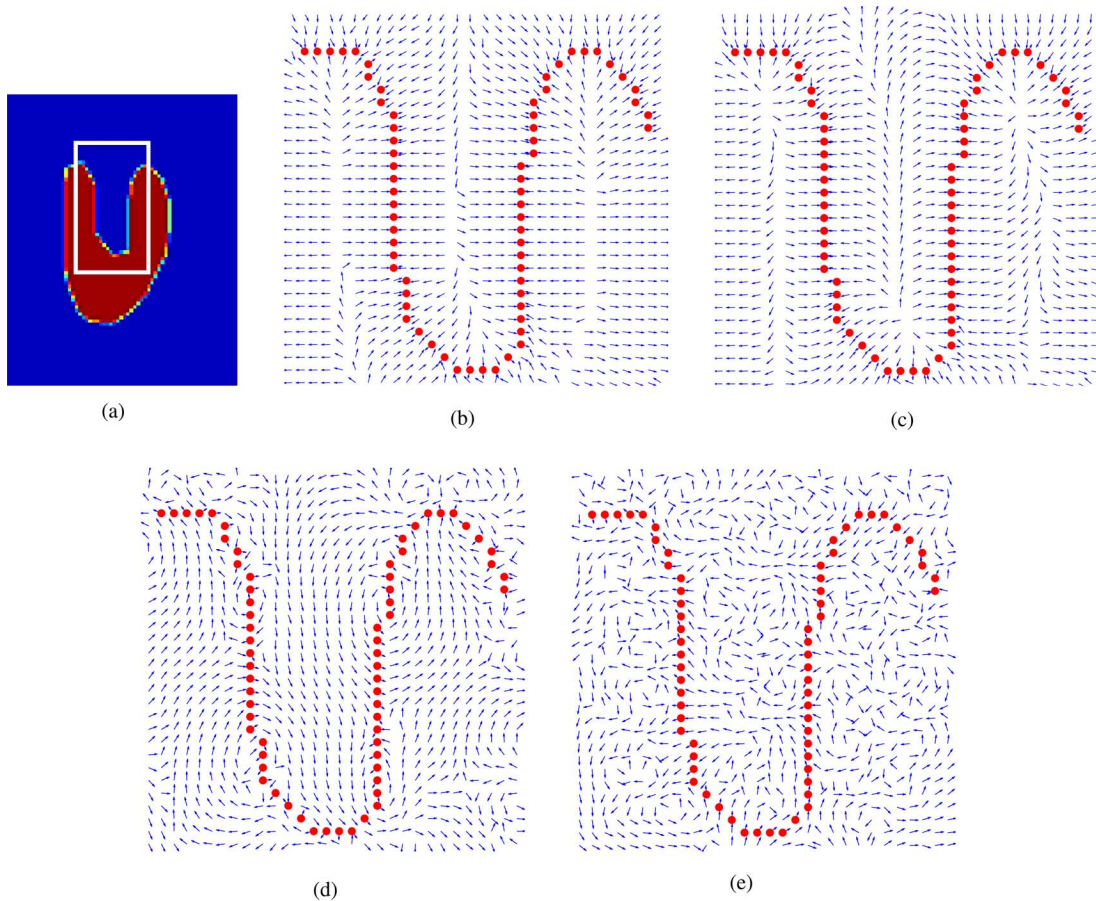


Fig. 5. This figure demonstrates the characteristics of the component flow fields for different cases. (a) A rectangular region of interest. The plot of (b) EFV field  $\mathbf{E}$  and (c) the conservative component of  $\mathbf{E}$ . The solenoidal components of (d)  $\mathbf{E}$  and (e) the GAC field. The maximum magnitudes of the field vectors are shown below each plot. (a) Max magnitude = 4.2. (b) Max magnitude = 1.2. (c) Max magnitude = 3.6. (d) Max magnitude =  $10^{-15}$ .

we obtain a smooth map [Fig. 3(c)] of the divergence of the flow field without losing its salient features (e.g., the position of local minima corresponding to edge locations). Consequently, the scalar potential  $\phi$ , after being scaled between 0 and 1, has small values (near zero) on the edges and close to one in the smooth regions. Fig. 4 makes a comparison between the traditional choice  $h = (1/1 + |\nabla I_\sigma|)$  and  $\phi(x, y)$  computed by solving the Poisson problem in (13) (with the edge flow field  $\mathbf{S}$  taken as EFV). Notice that  $\phi(x, y)$  localizes the edges better than the adhoc choice  $h$  (for both cases the image is smoothed with the same choice of scale parameter).

In summary, the curve evolution framework in (10) can be rewritten as

$$\frac{\partial C}{\partial t} = \alpha \phi \mathcal{N} + \beta \kappa \phi \mathcal{N} + (\mathbf{S} \cdot \mathcal{N}) \mathcal{N} \quad (17)$$

where  $\mathcal{N}$  is the unit inward normal to the curve;  $\kappa$  is curvature term; and  $\alpha$  and  $\beta$  are the constants. Equation (17) can be implemented through level set methods [17], [25].

Consider the binary image in Fig. 5(a) with a “U-shaped” object. We resolve different edge flow fields computed from this image using the Helmholtz-Hodge Decomposition. The field vectors computed from EFV inside the rectangular region of interest in Fig. 5(a) are shown in Fig. 5(b), and Fig. 5(d) shows the solenoidal component as per HHD (see Section III-A2). We can

observe that the solenoidal component of EFV points towards the concavities in the object. Note that the solenoidal component of GAC is close to zero (of the order of  $10^{-15}$ ), since it is purely conservative in nature. For ease of understanding, true edges are overlaid on the top of the flow fields in red dots.

Fig. 6 compares GAC and EFV-based segmentation starting with the circle as the initial condition for curve evolution [Fig. 6(a)]. Notice that purely conservative fields do not result in a good segmentation [Fig. 6(b) for GAC and Fig. 6(c) for the conservative component of EFV], and the nonconservative EFV results in almost perfect segmentation. One can expect similar result for the nonconservative GVF (see [31] for detailed explanations) as well. We now analytically show that EFV is nonconservative.

### B. EFV Is NonConservative

Consider

$$\mathbf{E}_s = |\nabla I \cdot \hat{v}_{\theta(x,y)}| e^{i\theta(x,y)} \quad (18)$$

where  $i = \sqrt{-1}$ ,  $\theta(x, y)$  provides the flow direction [see (8)] at each point, and  $\hat{v}_{\theta(x,y)}$  is a unit vector along that direction. This is essentially the term inside the integral in (9) without the Gaussian smoothing of the image. We will now show that this is a nonconservative field. The dropping of the Gaussian

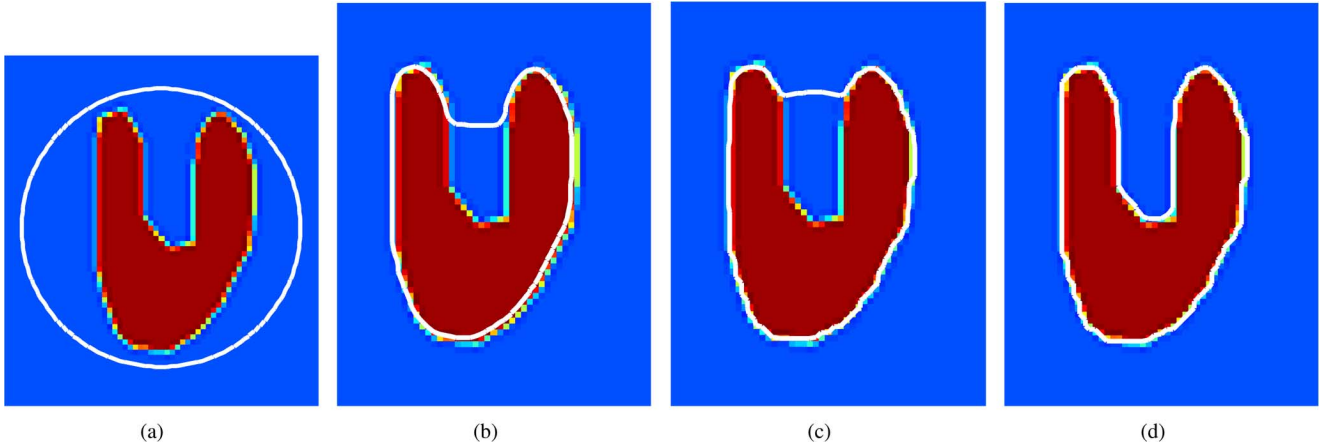


Fig. 6. (a) Initialization of the curve. The segmentation result with (b) GAC (c) the conservative component of EFV field (d)  $\mathbf{E}$ . The scale parameter  $\sigma$  is set to 1 for the calculation of flow fields for all these cases. Note that the GAC and the conservative component of  $\mathbf{E}$  are unable to produce desired segmentation results.

smoothing is for analytical simplification and does not affect the final conclusion. The integral, in some very special cases, may lead to an overall conservative field but would make the following analysis infeasible (recall that the integration is for smoothing purposes). Expanding (18), we obtain

$$\mathbf{E}_s = [I_x \cos(\theta(x, y)) + I_y \sin(\theta(x, y))](\cos(\theta(x, y)) + i \sin(\theta(x, y))) \quad (19)$$

where  $I_x$  and  $I_y$  are the partial derivatives in the  $x$  and  $y$  directions, respectively.

To prove that  $\mathbf{E}_s = [e_1(x, y), e_2(x, y)]$  is nonconservative, we need to show

$$\nabla \cdot \mathbf{E}_s \neq 0 \quad \text{and} \quad (20)$$

$$\nabla \times \mathbf{E}_s \neq 0. \quad (21)$$

As the variables involved are independent of  $z$ , these further simplify to

$$\frac{\partial e_1}{\partial x} \neq -\frac{\partial e_2}{\partial y} \quad \text{from Eq. (20) and} \quad (22)$$

$$\frac{\partial e_1}{\partial y} \neq \frac{\partial e_2}{\partial x} \quad \text{from Eq. (21)} \quad (23)$$

where

$$e_1 = \left( \frac{I_x}{2} + \frac{I_x}{2} \cos(2\theta(x, y)) + \frac{I_y}{2} \sin(2\theta(x, y)) \right)$$

and

$$e_2 = \left( \frac{I_y}{2} - \frac{I_y}{2} \cos(2\theta(x, y)) + \frac{I_x}{2} \sin(2\theta(x, y)) \right).$$

In obtaining these expressions for  $e_1$  and  $e_2$ , we assumed that  $I_x \cos(\theta(x, y)) + I_y \sin(\theta(x, y))$  in (19) is positive.<sup>3</sup> Since both  $I_x$  and  $I_y$  terms are present in both  $e_1$  and  $e_2$ , it is easy to see that (22) and (23) will always be satisfied. Thus,  $\mathbf{E}_s$  is nonconservative. As we discussed earlier it is reasonable to expect that

<sup>3</sup>It is straightforward to see that (22) and (23) remain unaltered with the sign inversion of the amplitude part as  $e_1$  and  $e_2$  both change their sign simultaneously in that case.

the smoothing operations involving the Gaussian filtering and the integration will not, in general, make the field conservative.

#### IV. COMPARISON OF EFV WITH GVF AND GGUF

Reasoning along the lines of the previous section, where we demonstrated that the EFV field is nonconservative, we can show that the nonconservative nature of the GVF field stems from the combination of the two terms: the edge enhancing  $|\nabla I|^2$  and the smoothing term  $(g_{1x}^2 + g_{1y}^2 + g_{2x}^2 + g_{2y}^2)$  in (1). It is important to note that either of the two terms alone would not result in a nonconservative field. For example, if we set  $\mu = 0$  in (1), the resulting field  $\mathbf{G}(x, y) = \nabla I$  is clearly conservative. On the other hand, replacing  $|\nabla I|^2$  with a constant coefficient would yield a conservative field as well. The smoothing in (1) is needed to extend the range of the vector field but has a detrimental effect on edge localization. This is illustrated in Fig. 7 for different cases of additive noise (from left to right the signal-to-noise ratios are 25, 20, 15, 10, and 5 dB) using the parameters suggested by [31] and fixing the scale at  $\sigma = 1$ . Notice that the localization of edges using EFV is not affected by noise even at signal-to-noise ratio (SNR) 5 dB, and this is due to the strong coupling of the edge stopping function which is derived from the image-based flow field vectors.

The poor edge localization of GVF is partially addressed in GGUF [see (3)] by the introduction of two spatially varying terms, e.g.,  $\eta_1(x, y)$  and  $\eta_2(x, y)$  (see Section II).  $\eta_1$  is small near edges and high away from the edges.  $\eta_2$  follows the opposite trend. Therefore, GGUF smooths intelligently unlike GVF which smooths equally everywhere. However, note that GGUF formulation is not directly obtained from an energy minimization like GVF. Consider the minimization of a new variational formulation

$$\int \int \eta_1 |\nabla \tilde{\mathbf{G}}|^2 + \eta_2 |\tilde{\mathbf{G}} - \nabla f|^2 dx dy \quad (24)$$

where  $\nabla \tilde{\mathbf{G}}$  is a second-order tensor. Note that the variational formulation in (1) is a special case of this (24) new variational formulation. The corresponding Euler equation is

$$\nabla \eta_1 \cdot \nabla \tilde{\mathbf{G}} + \eta_1 \nabla^2 \tilde{\mathbf{G}} - \eta_2 (\tilde{\mathbf{G}} - \nabla f) = 0. \quad (25)$$

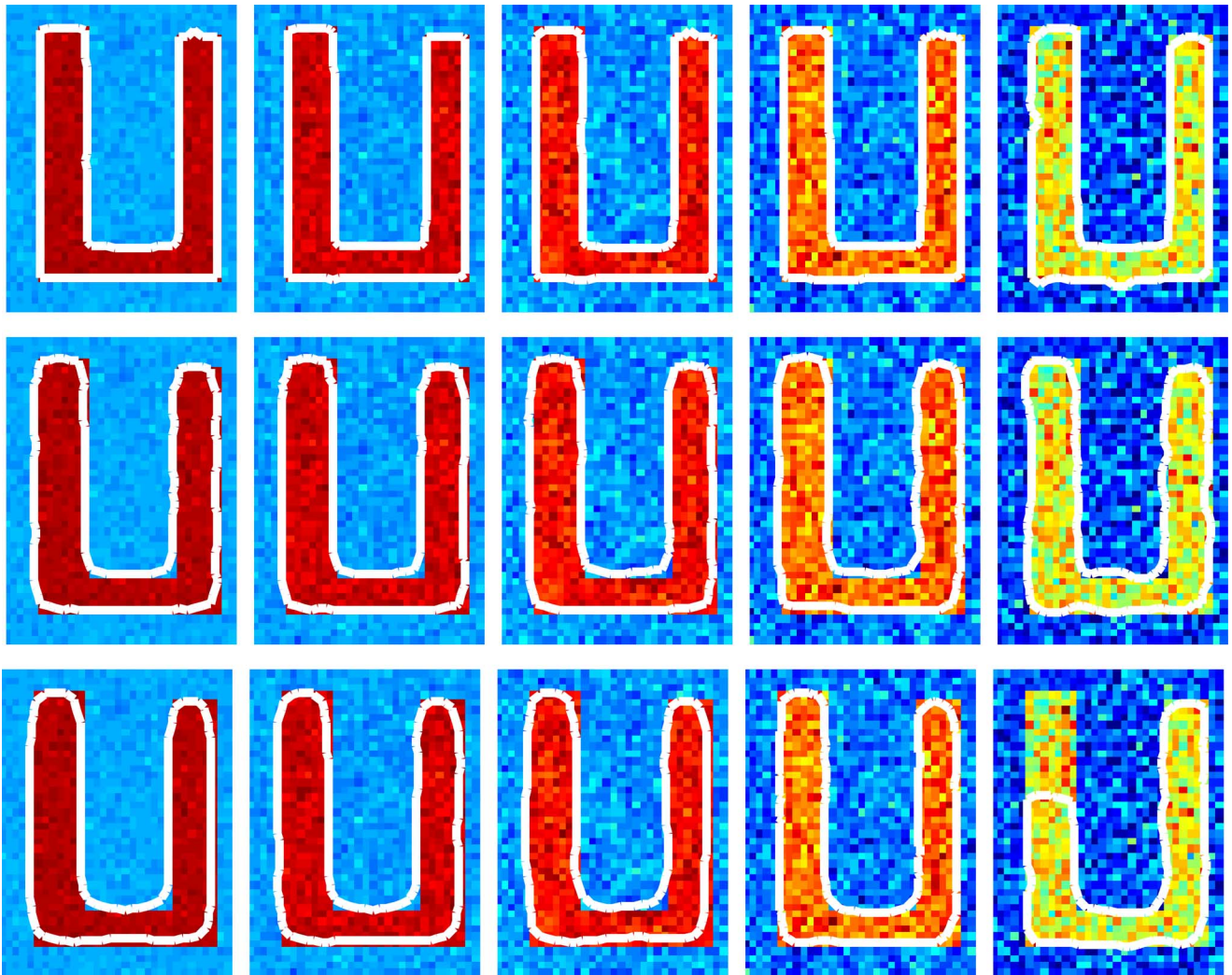


Fig. 7. This experiment demonstrates the edge localization property of EFV (first row), generalized GVF (second row), and GVF (third row) in presence of noise. The initialization is done as shown in Fig. 6(a), i.e., a circle surrounding the object of interest. The scale parameter  $\sigma$  is set to 1 for all methods. From left to right (in all the rows) the signal-to-noise ratios of these images are 25, 20, 15, 10, 5 dB. Note that the GVF and the Generalized GVF (GGVF) segmentation results are obtained using the parameter settings described by the authors in [31] and [30], respectively.

Equation (25) reduces to (3) if we assume  $\nabla\eta_1 \cdot \nabla\tilde{G} = 0$  which is generally not true near edges (may be satisfied in the homogenous regions). Also, retaining this term (i.e.,  $\nabla\eta_1 \cdot \nabla\tilde{G}$ ) can generate negative diffusion which leads to an ill posed PDE problem. The performance of GGVF on “U” images is shown in the second row of Fig. 7. EFV clearly outperforms both GGVF and GVF in terms of localizing the edges.

In addition, the smoothing term in GVF also contributes to poor localization in the presence of multicontrast edges, see Fig. 8(a), where a weaker (low contrast) edge is in close proximity of a stronger (higher contrast) edge. This was originally observed by Xie *et al.* [28], where the authors proposed to use a region-based flow in addition to the traditional edge-based flow used in GVF. Fig. 8(a) consists of nested squares with varying intensity values. The gray values are chosen in such a way that a couple of weak edges are kept deliberately in the vicinity of a strong edge. Fig. 8(d) and (e) show the GVF and EFV vectors, respectively, for the top right quarter of the image in Fig. 8(a). The opposing vectors are shown in different colors and the true edges are shown in green. GVF misses all the edges other than the innermost one between the

two innermost squares corresponding to the gray levels 0 and 255. These results confirm the earlier observation that high contrast edges do affect the detection of low contrast edges in the GVF formulation. Note that the EFV field is not affected by the presence of such multicontrast edges.

The issue of close proximity low contrast edges arises frequently in natural images, for example, see Fig. 9(a) which shows a small caterpillar lying on the stem of a shrub. The objective is to segment the caterpillar from the rest of the image. The EFV and the GVF fields are shown in Fig. 9(b) and (c) respectively. Again GVF (Fig. 9(e)) fails to detect the true edges whereas EFV effectively segments the caterpillar as shown in Fig. 9(d). For these experiments, the scale parameter  $\sigma$  is set to 0.5 for both methods. Moreover, we examine the GVF field for different values of  $\sigma$  (e.g., 1, 1.5, 2) and observed the same behavior as the plotted one [see Fig. 9(c)].

## V. EXPERIMENTAL RESULTS

In this section, we first provide a detailed comparison of the proposed EFV with three other state-of-the art approaches, namely,

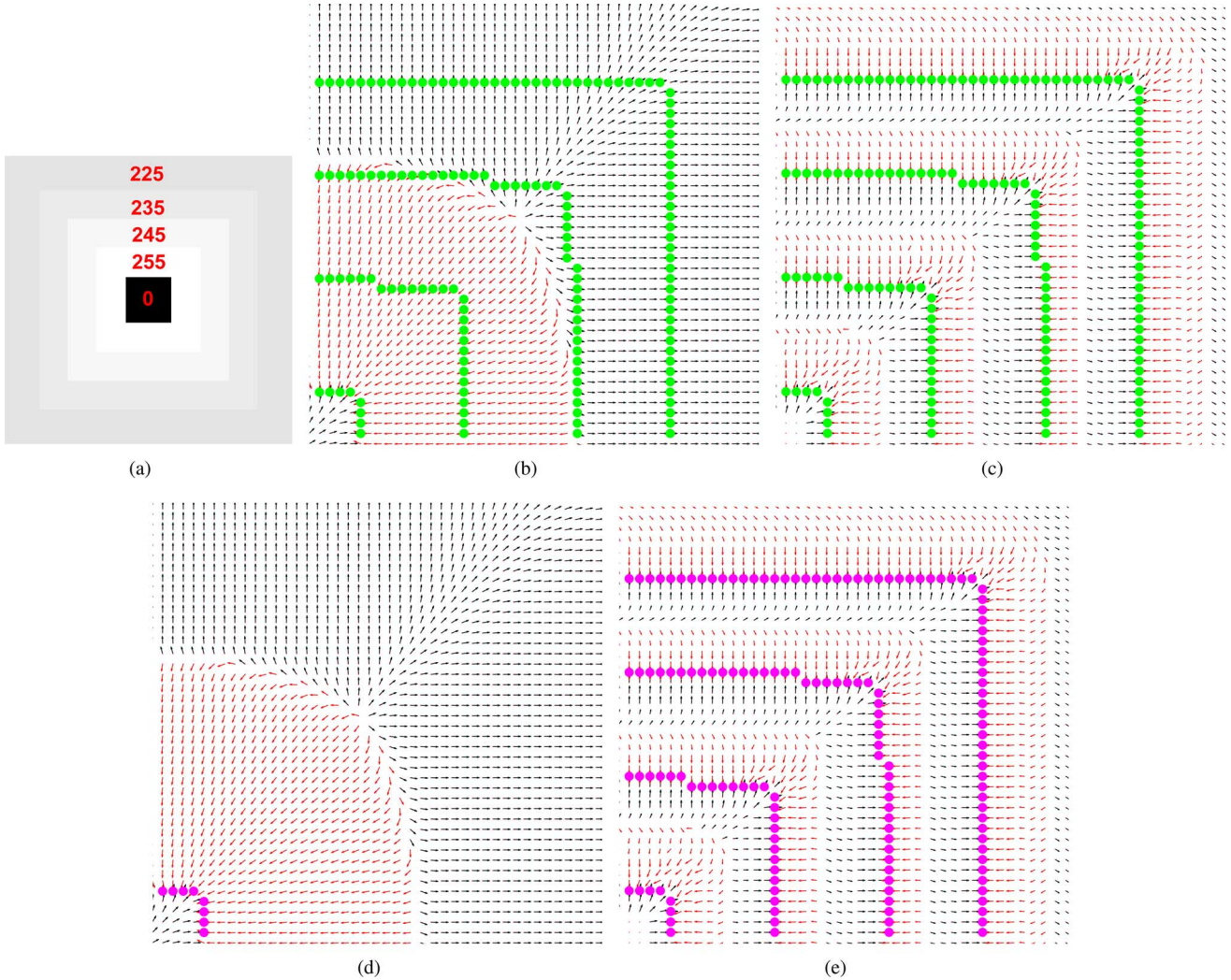


Fig. 8. This figure demonstrates the effect of the smoothing component in the GVF field formulation. (a) An example image. The gray values corresponding to each region are also shown. A close up view of the top right quarter of (b) GVF field, and (c) EFV field of the image. The true edges are plotted in green dots. Detected edges corresponding to (d) GVF field and (e) EFV field are shown in magenta dots. Note that the large capture range of the strongest edge suppressed all other weak edges for the case of GVF.

GAC, GVF, and GGVF. We also provide some qualitative results for MAC. MAC code can be downloaded from the authors' website.<sup>4</sup> We could not evaluate its performance on our large synthetic database of more than 1000 images since the user interface for the software only allows manually uploading and processing one image at a time and can not be used in batch mode.

Recall the general curve evolution equation:

$$\frac{\partial C}{\partial t} = \underbrace{\alpha a \mathcal{N}}_{\text{inflationary term}} + \underbrace{\beta a \kappa \mathcal{N}}_{\text{smoothing term}} + \underbrace{(\mathbf{S} \cdot \mathcal{N}) \mathcal{N}}_{\text{edge flow term}} \quad (26)$$

where  $\alpha$  and  $\beta$  are tuning parameters,  $\kappa$  is the curvature and  $\mathcal{N}$  is the normal to the curve. The scalar function  $a(x, y)$  and the vector field  $\mathbf{S}(x, y)$  differs for the four methods as follows:

- EFV:  $\mathbf{S} = \mathbf{E}$  and  $a = \phi$ , the scalar potential of  $\mathbf{E}$  (i.e.,  $\nabla \cdot \mathbf{E} = -\nabla^2 \phi$ );
- GGVF:  $\mathbf{S} = \mathbf{G}$  and  $a = h$ , where  $h = 1/(1 + |\nabla I_\sigma|)$ ;

<sup>4</sup><http://www.cs.swan.ac.uk/~csjason/snakes/mac/>.

- GVF:  $\mathbf{S} = \mathbf{G}$  and  $a = h$ .
- GAC:  $\mathbf{S} = -\nabla h$  and  $a = h$ .

Note that GGVF or GVF do not consider the inflationary term [see (26)] explicitly in their formulations. The reason is that the GGVF or GVF field have wider capture range. In principle the presence of this inflationary term, however, should not disturb the edge localization, since the edge stopping function  $a(x, y)$  reduces to zero near edges. This fact is true with the smoothing term (does not have any effect near edges) as well. Thus, only the edge flow term in (26) drives the contour near edges. Moreover, from our experience considering the inflationary term in the formulation provides faster convergence particularly in the presence of excessive noise.

We choose the SIID, Shape Image Database from Brown university [24], to demonstrate the effectiveness of the proposed framework in dealing with sharp junctions and corners. The collection is composed of 18 different shape categories. Each category has 12 different variations of the same shape for a total of 216 ( $18 \times 12$ ) images. For our experiments, we corrupted the images with additive white Gaussian noise; the SNRs

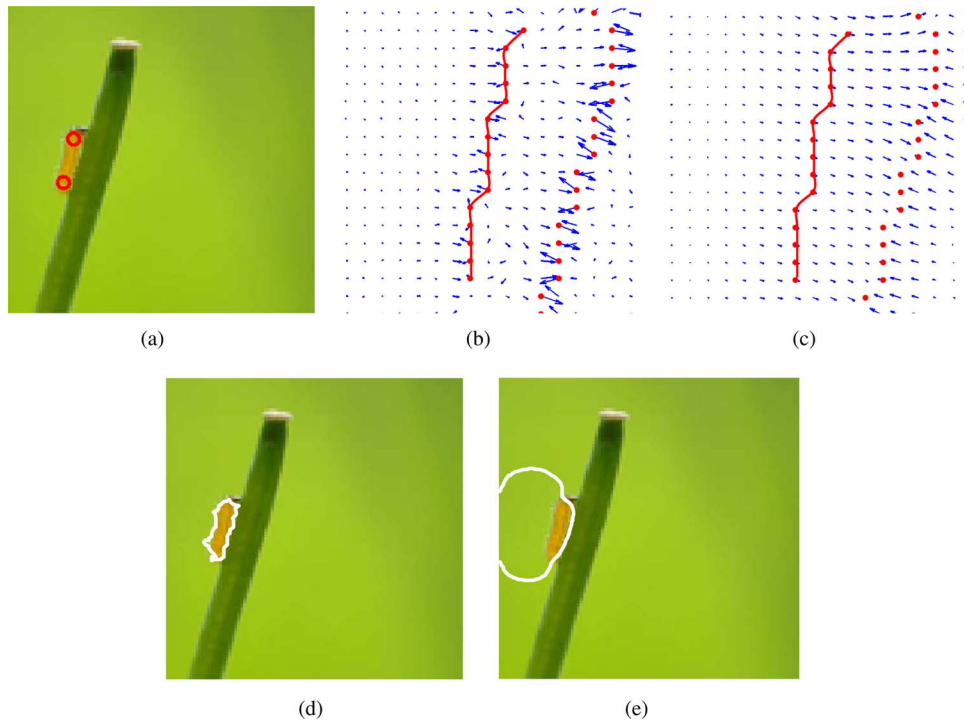


Fig. 9. Performance of EFV and GVF on closely located low contrast edges. A negligible amount of constant expansion force is applied for both methods to prevent the initialized contour from collapsing. (a) An image of a caterpillar where the red contour shows the initialization for both methods. The edge flow field corresponding to (b) EFV and (c) GVF. The back of the caterpillar [image courtesy of Dries Knapen (<http://www.focusonnature.be>)] is shown by connected red dots. The segmentation results using (d) EFV and (e) GVF field. Note that, in case of EFV, the vectors from opposite directions meet each other around the connected red dots whereas this is not true for GVF.

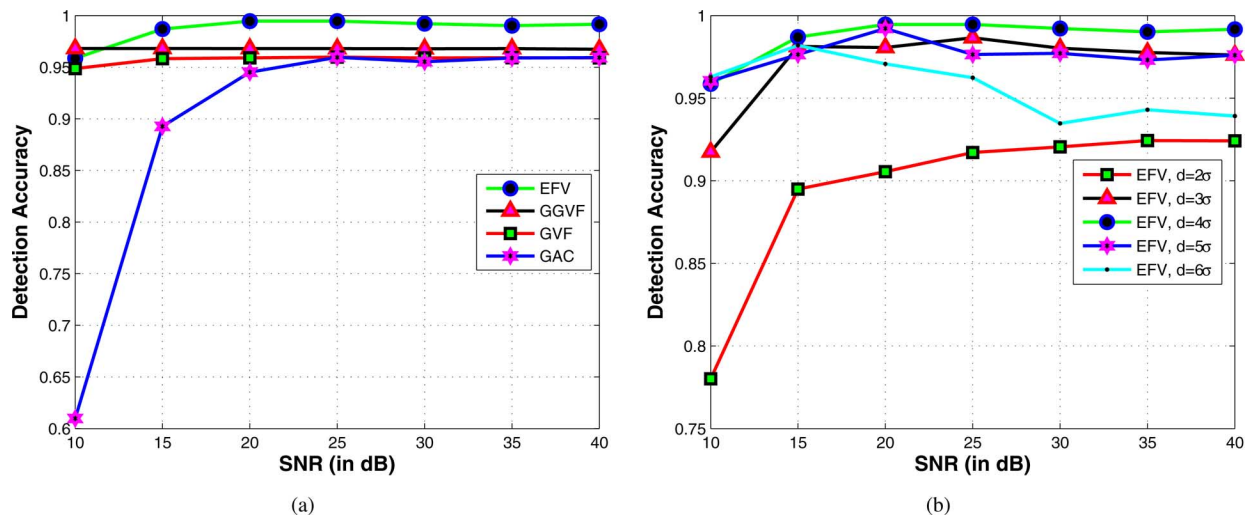


Fig. 10. (a) Comparison of edge localization using EFV ( $d = 4\sigma$ ), GGVF, GVF, GAC. (b) The performance of EFV with different settings of the offset parameter  $d$ .

are 10, 15, 20, 25, 30, 35, 40 dB, and then we compared different segmentation techniques. The scale parameter  $\sigma$  is set to 1 for all the methods. The detection accuracy is measured as:  $(|M_g \cap M_o| / |M_g \cup M_o|)$ , where  $M_g$  is the ground truth mask and  $M_o$  is the binary mask of the segmentation result. The maximum value is attained when the segmentation result exactly matches with the target. The parameters  $\alpha$  and  $\beta$  in (26) are tuned using a subset of the entire dataset, for each of the three segmentation methods separately. The computed parameters are kept fixed for the testing phase. The performance of different

methods is presented in Fig. 10(a). The results show that the EFV performs better than the other three techniques almost in all noise levels. Fig. 10(b) demonstrates the performance of EFV for different values of  $d$  (the offset parameter in the difference of offset Gaussian filter). As can be seen,  $d = 4\sigma$  provides a good trade-off between the edge localization and avoiding the noise interference. In Fig. 13, we present some qualitative results on a set of natural images. To capture the complex edges for these images, we decided to compute the multiscale version of EFV presented in Appendix A.

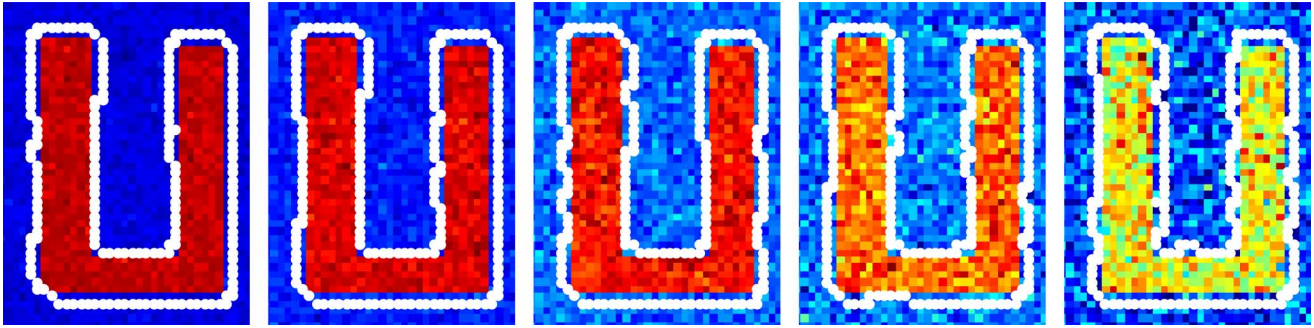


Fig. 11. Performance of magnetostatic active contour on noise corrupted U images.

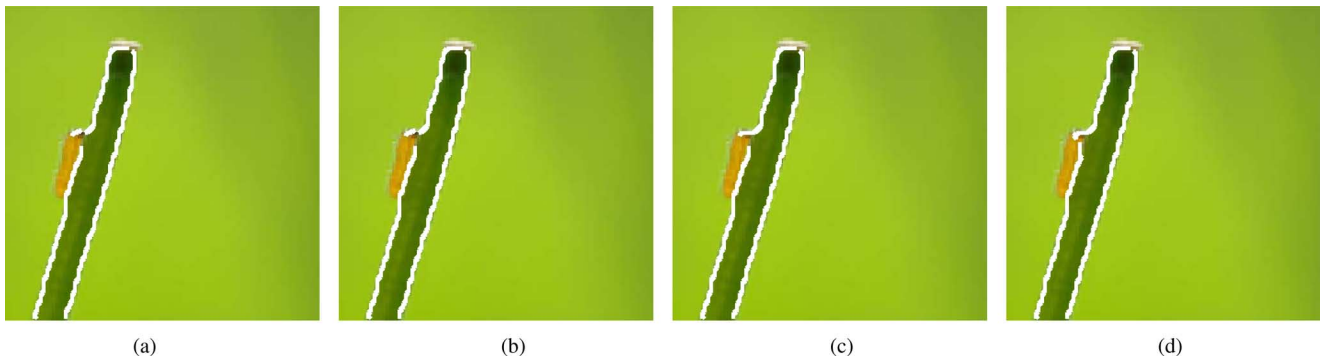


Fig. 12. Segmentation result (in white contour) using MAC for different setting of gradient threshold parameter  $\zeta$ . Note that the caterpillar is missed in all the cases. (a)  $\zeta = 0.1$  (default), (b)  $\zeta = 0.01$ , (c)  $\zeta = 0.001$ , (d)  $\zeta = 0.0001$ .

The authors in [29] investigated the initialization issue for the level set function elaborately. In contrast, we examine its edge localization and detection capability in presence of various challenges. The noise corrupted “U” images (Fig. 7) and the caterpillar image [Fig. 9(a)] are used to demonstrate the performance of MAC. The noise contents for the “U” images are kept the same as before (see Fig. 7). The initialization is done as shown in Fig. 6(a). The outputs (Fig. 11) are obtained directly from the software developed by the authors [29]. The software returns two level-set functions, one for localizing the object and another for localizing the background. We only show the contour which localizes the object. The results demonstrate that MAC is unable to localize the edges precisely (see the EFV results in the first row of Fig. 7 for comparison). We use the default parameter setting for these experiments. The default parameter setting in MAC assigns full weight to the smoothing term and it completely ignores the data term (see (26)), resulting in a poor edge localization. Assigning more weight to the data term seems to improve edge localization but results in more false positives. Fig. 12 demonstrates the performance of MAC on the caterpillar image. The same initialization is used as shown in Fig. 9(a). These results are obtained by varying the gradient threshold parameter,  $\zeta$ .  $\zeta$  is a parameter which removes noisy edges (see [29] for detailed explanations) after initial edge computation. The default setting (provided by the authors) is used for rest of the parameters. In all the cases, the contours wrongly latch onto the dominant object, i.e., the stem.

## VI. CONCLUSION

We explored the properties of a nonconservative edge flow field, EFV, for robust image segmentation. The nonconservative nature of EFV is demonstrated both analytically and numerically. We showed that the nonconservative nature of the edge flow field is critical in detecting boundaries of objects with concavities. In incorporating the EFV into the curve evolution framework, we derived a new edge stopping function analytically from the EFV in a principled way. We showed that this edge stopping function is better than the traditionally used inverse of the gradient magnitude function in terms of edge localization. We compared the EFV with well known state-of-the-art approaches, providing detailed experimental results that demonstrated the advantage of EFV over other methods. In this paper our work addresses the single object segmentation problem. Future work include extensions to multiple object segmentation and a principled approach to the multiscale framework.

## APPENDIX A MULTISCALE EFV FIELD

We adopt a fine to coarse strategy to compute the multiscale EFV where the flow field is first derived at the finest scale (say at  $s_1$ ) and then the flow vectors are selectively modified using the ones from the coarser scales. The procedure is presented in Algorithm 1.



Fig. 13. This figure presents the effectiveness of EFV on complex natural images.

---

**Algorithm 1** Algorithm for computing multiscale intensity-based EdgeFlow. In the experiments we choose  $s_1 = 0.5$ ,  $s_2 = 2$ ,  $\Delta s = 0.5$ ,  $\theta = 45^\circ$  and  $\gamma = 1/15$

---

Consider  $I(x, y)$  be an image. Let  $\gamma$  and  $\theta$  be the threshold values for the edge magnitude and the angle respectively. Let  $s_1$  and  $s_2$  be the finest and coarsest scale considered with a step size of  $\Delta s$ .

$\mathbf{E} = \text{EdgeFlow}(I, s_1)$ .

Set  $s = s_1$ .

**while**  $s < s_2$  **do**

    Set  $s = s + \Delta s$

$\mathbf{T} = \text{EdgeFlow}(I, s)$ .

$M = \text{Max}(\|\mathbf{E}\|)$

**for all** pixels in  $I(x, y)$  **do**

**if**  $\|\mathbf{E}(x, y)\| < \gamma \cdot M$  **then**

$\mathbf{E}(x, y) = \mathbf{T}(x, y)$

**else if**  $\text{Angle}(\mathbf{E}(x, y), \mathbf{T}(x, y)) < \theta$  **then**

$\mathbf{E}(x, y) = \mathbf{E}(x, y) + \mathbf{T}(x, y)$

**else**

$\mathbf{E}(x, y)$  is kept the same.

**end if**

**end for**

**end while**

#### APPENDIX B

##### SOLUTION FOR THE SCALAR POTENTIAL

Consider  $\Gamma$  be a closed domain in  $\mathbb{R}^2$  with boundary  $\partial\Gamma$ . Let  $\mathbf{E}$  be a smoothly varying vector field defined in  $\Gamma$ . Find the

optimum solution for the following functional:

$$\min_{\phi} \int_{\Gamma} \|\mathbf{E} - \nabla\phi\|^2 dA. \quad (27)$$

*Proof:* Using calculus of variation this problem can be solved as follows:

$$\frac{\partial}{\partial \epsilon} \left( \int_{\Gamma} \|\mathbf{E} - \nabla(\phi + \epsilon\psi)\|^2 dA \right) \Big|_{\epsilon=0} = 0$$

$$2 \int_{\Gamma} (\mathbf{E} - \nabla(\phi + \epsilon\psi)) \cdot \nabla\psi dA \Big|_{\epsilon=0} = 0$$

$$\int_{\Gamma} (\mathbf{E} - \nabla\phi) \cdot \nabla\psi dA = 0.$$

Now applying integration by parts, we obtain

$$\int_{\partial\Gamma} (\mathbf{E} - \nabla\phi) \cdot \mathbf{n} - \int_{\Gamma} (\nabla \cdot \mathbf{E} - \nabla^2\phi) \psi dA = 0.$$

Assuming proper boundary condition and the fact that this relation should hold for any variation of  $\psi$ , the problem reduces to solving the following PDE:

$$\nabla \cdot \mathbf{E} = \nabla^2\phi \text{ in } \Gamma \subset \mathbb{R}^2$$

with

$$(\mathbf{E} - \nabla\phi) \cdot \hat{\mathbf{n}} = 0 \text{ in } \partial\Gamma$$

where  $\hat{\mathbf{n}}$  is the unit outward normal to  $\partial\Gamma$ . ■

#### APPENDIX C

##### SOLUTION FOR THE VECTOR POTENTIAL

Find  $\mathbf{A}$  which minimizes the following functional in a given region  $\Omega \subset \mathbb{R}^3$

$$\min_{\mathbf{A}} \int_{\Omega} \|\mathbf{E} - (\nabla \times \mathbf{A})\|^2 dV. \quad (28)$$

*Proof:* The optimal solution can be obtained using calculus of variation as follows:

$$\begin{aligned} \frac{\partial}{\partial \epsilon} \left( \int_{\Omega} \|\mathbf{E} - \nabla \times (\mathbf{A} + \epsilon \mathbf{B})\|^2 dV \right) \Big|_{\epsilon=0} &= 0 \\ \left( 2 \int_{\Omega} (\mathbf{E} - \nabla \times (\mathbf{A} + \epsilon \mathbf{B})) \cdot (\nabla \times \mathbf{B}) dV \right) \Big|_{\epsilon=0} &= 0 \\ \int_{\Omega} (\mathbf{E} - \nabla \times \mathbf{A}) \cdot (\nabla \times \mathbf{B}) dV &= 0 \\ \int_{\Omega} \mathbf{E} \cdot \nabla \times \mathbf{B} dV - \int_{\Omega} (\nabla \times \mathbf{A}) \cdot (\nabla \times \mathbf{B}) dV &= 0. \end{aligned}$$

Now applying the identity from Lemma D.1 the above equality reduces to

$$\begin{aligned} \int_{\Omega} (\nabla \times \mathbf{E}) \cdot \mathbf{B} dV - \int_{\partial\Omega} (\mathbf{E} \times \mathbf{B}) \cdot d\mathbf{S} + \\ - \int_{\Omega} (\nabla \times \nabla \times \mathbf{A}) \cdot \mathbf{B} dV - \int_{\partial\Omega} (\mathbf{B} \times (\nabla \times \mathbf{A})) \cdot d\mathbf{S} &= 0 \end{aligned}$$

combining similar terms corresponding to the domain  $\Omega$  and the boundary  $\partial\Omega$ , we obtain

$$\begin{aligned} \int_{\Omega} (\nabla \times (\mathbf{E} - \nabla \times \mathbf{A})) \cdot \mathbf{B} dV \\ + \int_{\partial\Omega} (\mathbf{B} \times (\mathbf{E} - \nabla \times \mathbf{A})) \cdot d\mathbf{S} &= 0 \end{aligned}$$

after rearranging the terms this reduces to

$$\begin{aligned} \int_{\Omega} (\nabla \times \mathbf{E} - \nabla \times \nabla \times \mathbf{A}) \cdot \mathbf{B} dV \\ + \int_{\partial\Omega} ((\mathbf{E} - \nabla \times \mathbf{A}) \times \hat{n}) \cdot \mathbf{B} dS &= 0 \end{aligned}$$

where  $\hat{n}$  is the unit outward normal to  $\partial\Omega$ . Now letting the boundary condition be

$$((\mathbf{E} - \nabla \times \mathbf{A}) \times \hat{n}) = 0 \quad \text{in } \partial\Omega$$

we obtain

$$\int_{\Omega} (\nabla \times \mathbf{E} - \nabla \times \nabla \times \mathbf{A}) \cdot \mathbf{B} dV = 0. \quad (29)$$

As this relation must hold for any arbitrary  $\mathbf{B}$  we obtain the following PDE formulation to solve for  $\mathbf{A}$ :

$$\nabla \times \mathbf{E} = \nabla \times \nabla \times \mathbf{A} \quad \text{in } \Omega \subset \mathbb{R}^3. \quad \blacksquare$$

#### APPENDIX D

##### PROOF OF A VECTOR CALCULUS IDENTITY

*Lemma D.1:* Consider  $\Omega$  be a closed region in  $\mathbb{R}^3$  with boundary  $\partial\Omega$ . The following identity is valid for any arbitrary smooth vector fields  $\mathbf{F}$  and  $\mathbf{G}$  defined in  $\Omega$

$$\begin{aligned} \int_{\partial\Omega} [\mathbf{F} \times (\nabla \times \mathbf{G})] \cdot d\mathbf{S} &= \int_{\Omega} (\nabla \times \mathbf{F}) \cdot (\nabla \times \mathbf{G}) dV \\ &- \int_{\Omega} \mathbf{F} \cdot (\nabla \times \nabla \times \mathbf{G}) dV. \quad (30) \end{aligned}$$

*Proof:* Applying Gauss divergence theorem on the left hand side of (30), we obtain

$$\begin{aligned} \int_{\partial\Omega} [\mathbf{F} \times (\nabla \times \mathbf{G})] \cdot d\mathbf{S} &= \int_{\Omega} \nabla \cdot [\mathbf{F} \times (\nabla \times \mathbf{G})] dV \\ &= \int_{\Omega} (\nabla \times \mathbf{F} \cdot \nabla \times \mathbf{G} - \mathbf{F} \cdot (\nabla \times \nabla \times \mathbf{G})) dV. \quad (31) \end{aligned}$$

This completes the proof. Note that the last step follows from the following vector calculus identity:

$$\nabla \cdot (\mathbf{A} \times \mathbf{B}) = (\nabla \times \mathbf{A}) \cdot \mathbf{B} - \mathbf{A} \cdot (\nabla \times \mathbf{B}). \quad \blacksquare$$

#### ACKNOWLEDGMENT

The authors would like to thank all the anonymous reviewers for their valuable comments and thoughtful suggestions which improved the quality of the presented work.

#### REFERENCES

- [1] M. S. Allili and D. Ziou, A Robust Video Object Tracking by Using Active Contours, 2006.
- [2] V. Caselles, R. Kimmel, and G. Sapiro, "Geodesic active contours," *Int. J. Comput. Vis.*, vol. 22, no. 1, pp. 61–80, Feb. 1997.
- [3] T. Chan, B. Y. Sandberg, and L. Vese, "Active contours without edges for vector-valued images," *J. Vis. Commun. Image Represent.*, vol. 11, pp. 130–141, 2000.
- [4] T. F. Chan and L. A. Vese, "Active contours without edges," *IEEE Trans. Image Process.*, vol. 10, no. 2, pp. 266–77, Feb. 2001.
- [5] Q. Chena, Q. Suna, P. Hengb, and D. Xiaa, "Parametric active contours for object tracking based on matching degree image of object contour points," *Pattern Recognit. Lett.*, pp. 126–141, Jan. 2008.
- [6] L. D. Cohen and I. Cohen, "Finite-element methods for active contour models and balloons for 2-d and 3-d images," *IEEE Trans. Pattern Anal. Mach. Intell.*, pp. 1131–1147, Nov. 1993.
- [7] A. Dufour, V. Shinin, S. Tajbakhsh, N. Guillen-Aghion, J.-C. Olivo-Marin, and C. Zimmer, "Segmenting and tracking fluorescent cells in dynamic 3-d microscopy with coupled active surfaces," *IEEE Trans. Image Process.*, vol. 14, no. 9, pp. 1396–1410, Sep. 2005.
- [8] D. Gil and P. Radeva, "Curvature vector flow to assure convergent deformable models for shape modelling," in *Proc. EMMCVPR*, 2003, pp. 357–372.
- [9] M. Kass, A. Witkin, and D. Terzopoulos, "Snakes: Active contour models," *Int. J. Comput. Vis.*, pp. 321–331, 1988.
- [10] S. Kichenassamy, A. Kumar, P. Olver, A. Tannenbaum, and A. Yezzi, "Gradient flows and geometric active contour models," in *Proc. Int. Conf. Computer Vision*, Jun. 1995, pp. 810–815.
- [11] F. Lempelius and J. Pauli, "Active contour based object detection," in *Proc. Int. Conf. Pattern Recognition and Information Processing*, 1997, pp. 171–175.
- [12] B. Leroy, I. Herlin, and L. D. Cohen, "Multiresolution algorithms for active contour models," in *Proc. 12th Int. Conf. Analysis and Optimization of Systems*, 1996, pp. 58–65.
- [13] M. Leventon, W. Grimson, and O. Faugeras, "Statistical shape influence in geodesic active contours," in *Proc. IEEE Conf. Computer Vision and Pattern Recognition*, 2000, pp. 316–323.
- [14] W.-Y. Ma and B. S. Manjunath, "Edgeflow: A technique for boundary detection and image segmentation," *IEEE Trans. Image Process.*, pp. 1375–1388, Aug. 2000.
- [15] R. Malladi, J. A. Sethian, and B. C. Vemuri, "Evolutionary fronts for topology-independent shape modeling and recovery," in *Proc. Eur. Conf. Computer Vision*, 1994, pp. 3–13.
- [16] J. Marsden and A. Tromba, *Vector Calculus*, 3rd ed. New York: W.H. Freeman, 1996.
- [17] S. Osher and J. A. Sethian, "Fronts propagating with curvature-dependent speed: Algorithms based on Hamilton–Jacobi formulations," *J. Comput. Phys.*, vol. 79, pp. 12–49, 1988.
- [18] N. Paragios and R. Deriche, "Geodesic active contours and level sets for the detection and tracking of moving objects," *IEEE Trans. Pattern Anal. Mach. Intell.*, pp. 266–280, Mar. 2000.

- [19] N. Paragios and R. Deriche, "Geodesic active regions and level set methods for supervised texture segmentation," *Int. J. Comput. Vis.*, pp. 223–247, Feb. 2002.
- [20] N. Paragios, O. Mellina-Gottardo, and V. Ramesh, "Gradient vector flow fast geometric active contours," *IEEE Trans. Pattern Anal. Mach. Intell.*, pp. 402–407, Mar. 2004.
- [21] N. Paragios, O. Mellina-Gottardo, and V. Ramesh, "Gradient vector flow fast geometric active contours," *IEEE Trans. Pattern Anal. Mach. Intell.*, pp. 402–407, Mar. 2004.
- [22] C. Pluempitwiriyawej, J. Moura, Y. Wu, and C. Ho, "Stacs: New active contour scheme for cardiac mr image segmentation," *IEEE Trans. Med. Imag.*
- [23] K. Polthier and E. Preub, "Variational approach to vector field decomposition, scientific visualization," presented at the Eurographics Workshop on Scientific Visualization, 2000.
- [24] T. B. Sebastian, P. N. Klein, and B. B. Kimia, "Recognition of shapes by editing shock graphs," in *Proc. ICCV*, 2001, pp. 755–762.
- [25] J. A. Sethian, *Level Set Methods and Fast Marching Methods: Evolving Interfaces in Computational Geometry, Fluid Mechanics, Computer Vision, and Materials Science*. Cambridge, MA: Cambridge Univ. Press, 1999.
- [26] A. Tsai, A. Yezzi, W. Wells, C. Tempany, D. Tucker, A. Fan, W. Grimson, and A. Willsky, "A shape based approach to the segmentation of medical imagery using level sets," *IEEE Trans. Med. Imag.*, vol. 22, no. 2, pp. 137–154, 2003.
- [27] Y. Xiang, A. C. S. Chung, and J. Ye, "An active contour model for image segmentation based on elastic interaction," *J. Comput. Phys.*, vol. 219, pp. 455–476, Nov. 2006.
- [28] X. Xie and M. Mirmehdi, "Rags: Region-aided geometric snake," *IEEE Trans. Image Process.*, pp. 640–652, May 2004.
- [29] X. Xie and M. Mirmehdi, "Mac: Magnetostatic active contour model," *IEEE Trans. Pattern Anal. Mach. Intell.*, vol. 30, no. 4, pp. 632–646, 2008.
- [30] C. Xu and J. Prince, "Generalized gradient vector flow external forces for active contours," *Signal Process.*, pp. 131–139, Dec. 1998.
- [31] C. Xu and J. L. Prince, "Snakes, shapes, and gradient vector flow," *IEEE Trans. Image Process.*, pp. 359–369, Mar. 1998.
- [32] S. C. Zhu and A. Yuille, "Region competition: Unifying snakes, region growing, and bayes/mdl for multiband image segmentation," *IEEE Trans. Pattern Anal. Mach. Intell.*, pp. 884–900, Sep. 1996.



**Pratim Ghosh** (S'08) was born in West Bengal, India, in 1981. He received the B.E. degree in electrical engineering from Jadavpur University, Kolkata, India, in 2004, and the M.E. degree in system science and automation (with distinction) from the Indian Institute of Science, Bangalore, in 2006. He is currently pursuing the Ph.D. degree in the Department of Electrical and Computer Engineering, University of California, Santa Barbara.

He interned at Janelia Farm, Howard Hughes Medical Institute, in the summer of 2009. His research interests span the areas of computer vision and pattern recognition with particular emphasis on variational methods for image segmentation.



**Luca Bertelli** (S'04) received the D.Eng. degree (*summa cum laude*) in electronic engineering from the University of Modena, Italy, in 2003, and the M.S. and Ph.D. degrees in electrical and computer engineering from the University of California, Santa Barbara, in 2005 and 2009, respectively.

During the summer of 2008, he was an intern at Google Research in Mountain View, CA, working on salient object detection. He is currently a Research Staff Member at Mayachitra, Inc., Santa Barbara. His research interests include variational methods for image segmentation, level set methods, shape-based segmentation, and other aspects of computer vision and machine learning.



**Baris Sumengen** received the B.S. degree from Bogazici University, Turkey, in both electrical engineering and mathematics in 1998 and the M.S. degree in 2000 and the Ph.D. degree in 2004 in electrical and computer engineering from University of California, Santa Barbara (UCSB).

From 2004 to 2005, he was a postdoctorate at the UCSB Center for bio-image informatics. Since 2006, he has been with Like.com (formerly Riya) as a research architect leading the design of scalable content based image similarity engines. His primary research interests include image segmentation, content-based image retrieval, and data mining in large multimedia databases.



**B. S. Manjunath** (F'05) received the B.E. degree in electronics (with distinction) from the Bangalore University, India, in 1985, the M.E. degree (with distinction) in systems science and automation from the Indian Institute of Science in 1987, and the Ph.D. degree in electrical engineering from the University of Southern California, Los Angeles, in 1991.

He is now a Professor of electrical computer engineering and Director of the Center for Bio-Image Informatics at the University of California, Santa Barbara. His current research interests include image processing, data hiding, multimedia databases, and bio-image informatics. He is a coeditor of the book *Introduction to MPEG-7* (Wiley, 2002).

Dr. Manjunath was a recipient of the national merit scholarship (1978–1985) and was awarded the university gold medal for the best graduating student in electronics engineering in 1985 from the Bangalore University. He was an associate editor of the *IEEE Transactions Image Processing* and is currently an Associate Editor of the *IEEE TRANSACTIONS ON PATTERN ANALYSIS AND MACHINE INTELLIGENCE* and the *IEEE TRANSACTIONS ON MULTIMEDIA*.